Impacts of oxygen vacancies on the electrocatalytic activity of AuTiO$_2$ nanocomposites towards oxygen reduction

CrossMark

Samantha W. Sweeney [a], Graham Roseman [a], Christopher P. Deming [a], Nan Wang [b], Tuan Anh Nguyen [a], Glenn L. Millhauser [a], Shaowei Chen [a,*]

[a] Department of Chemistry and Biochemistry, University of California, 1156 High Street, Santa Cruz, CA 95064, USA
[b] New Energy Research Institute, School of Environment and Energy, South China University of Technology, Guangzhou Higher Education Mega Centre, Guangzhou 510006, China

ARTICLE INFO

ABSTRACT

Nanocomposites based on metal nanoparticles supported on oxide surfaces have been used extensively as effective catalysts for fuel cell electrochemistry. In this study, functional nanocomposites based on gold nanoparticles deposited onto TiO$_2$ colloids were prepared by a simple wet chemistry method, and subject to hydrothermal treatment at a controlled temperature in the presence of ascorbic acid. Transmission electron microscopic measurements showed that the gold nanoparticles (10–30 nm in diameter) were embedded within the TiO$_2$ matrix consisting of colloids of 5–10 nm in diameter and anatase crystalline structures, as evidenced in x-ray diffraction studies. Interestingly, electron paramagnetic resonance measurements showed the formation of oxygen vacancies after hydrothermal treatment and the concentrations of oxygen vacancies increased with the amount of ascorbic acid added. Consistent results were obtained in x-ray photoelectron spectroscopic measurements, which suggested partial charge transfer from gold to oxygen-deficient TiO$_2$. The Au:Ti atomic ratio in the nanocomposites was estimated to be ca. 11% and consistent among the series of samples. Electrochemically, the nanocomposites exhibited apparent electrocatalytic activity towards oxygen reduction reactions in alkaline media, which showed a peak-shaped variation with the concentration of the oxygen vacancies. This was accounted for by the deliberate manipulation of the binding energy of oxygen species onto the nanocomposite surfaces. In addition, the AuTiO$_2$ nanocomposites exhibited markedly enhanced tolerance against methanol crossover, as compared to commercial Pt/C catalysts.

© 2016 Hydrogen Energy Publications LLC. Published by Elsevier Ltd. All rights reserved.

Introduction

Nanocomposites based on metal nanoparticles supported on oxide surfaces have been used extensively as effective catalysts for a wide range of chemical reactions, including fuel cell electrochemistry. In fact, such functional hybrid materials have been found to exhibit apparent electrocatalytic activity towards both oxidation of fuel molecules at the anode and reduction of oxygen at the cathode, with catalytic

---

performances comparable, or even superior, to that of state-of-the art platinum catalysts [1–4]. This has been ascribed largely to the strong metal-support interactions [5–9]. For instance, Comotti and co-workers deposited gold nanoparticles on various metal oxides and found that the electrocatalytic activity towards CO oxidation varied with the oxide support, with $AuTiO_2$ identified as the best catalyst among the series [10]. In another study [11], Lin et al. prepared a series of $AuTiO_2$ nanocomposites and identified an optimal gold loading for maximal activity towards oxygen reduction reactions (ORR), which was accounted for by the dependence of surface OH concentration on gold contents. Similarly, Chen and co-workers deposited gold on SnO_2 nanoparticles, and observed that the gold loading played a vital role in the determination of the electrocatalytic activity towards ORR [12]. With an increasing gold loading, the ORR evolved from a two-electron pathway to a four-electron one, and Tafel analysis showed that the optimal gold loading was ca. 1.9 at.% [12].

In these earlier studies, it is generally difficult to control the deposition and dispersion of metal nanoparticles on the oxide surfaces [13–15]. Horvath et al. [16] employed two different methods to mitigate such an issue. In the first method, TiO_2 was deposited onto gold colloid surface by hydrolysis of a titanium-alkoxide precursor and the resulting core@shell nanostructures were then adsorbed onto a SiO_2 surface by electrostatic interactions. In the second method, gold colloids were grown onto the SiO_2 surface, and then a layer of TiO_2 was coated onto the composite by controlled hydrolysis. The resulting $AuTiO_2/SiO_2$ nanocomposites were much more stable than the $AuTiO_2$ counterparts, and their CO oxidation activity was markedly higher than the $AuSiO_2$ reference sample. This was attributed to the controlled growth of the $AuTiO_2$ interface [16]. In another study [17], Ma and co-workers deposited SiO_2 onto $AuTiO_2$ nanocomposites, which also exhibited enhanced catalytic activity and stability for CO oxidation, as compared to $AuTiO_2$ alone. Similarly, Huang and co-workers successfully coated gold nanoparticles with ZrO_2 or TiO_2 through an assembly approach, and these "nanoreactors" were found to exhibit superior catalytic activity for CO oxidation, due to their porous structure and enhanced stability, as compared to the uncoated ones [18].

However, metal oxides typically exhibit only low electrical conductivity, which is detrimental to the electron-transfer reactions on the catalyst surface. To increase metal oxide conductivity, a number of methods have been reported in the literature. These include manipulation of the oxide crystallinity [19,20], doping [21–23], combination with carbon substrates [24,25], and introduction of oxygen vacancies into the oxide structure [26]. Of these, Linh and co-workers carried out DFT calculations to examine the impacts of oxygen vacancies in TiO_2 on oxygen adsorption, and found that the formation of oxygen vacancies enhanced the adsorption of oxygen species because of an increase of the oxygen binding energy [27]. Aschauer and co-workers also showed that oxygen adsorption might be enhanced by defect electrons transferring in the TiO_2 surface band gap [28]. Thus, one immediate question arises. Will the ORR electrocatalytic activity be enhanced by the formation of oxygen vacancy in the oxide support?

Note that thus far experimental studies have been scarce that focus on the impacts of TiO_2 oxygen vacancies on the ORR

activity of metal-TiO_2 nanocomposites. This is the primary motivation of the present study. Herein, we prepared a series of $AuTiO_2$ nanocomposites by colloidal chemistry, and the concentration of oxygen vacancy in TiO_2 was deliberately manipulated by hydrothermal heating [29] and ascorbic acid reduction [30], and evaluated by electron paramagnetic resonance measurements. Electrochemical measurements showed that the nanocomposites exhibited apparent ORR activity in alkaline media, which displayed a volcano-shaped variation with the TiO_2 oxygen vacancies. The optimal nanocomposites were found to exhibit an ORR activity that was comparable to that of commercial platinum catalysts, along with enhanced tolerance against methanol crossover.

Experimental section

Chemicals

Titanium(IV)-*tert*-butoxide (97%, Sigma–Aldrich), hydrogen tetrachloroauric acid ($HAuCl_4$, Sigma–Aldrich), oleic acid (≥99%, Sigma–Aldrich), 3-chloroaniline (≥99.0%, Sigma–Aldrich), sodium borohydride (≥98%, Sigma–Aldrich), and ascorbic acid (99.0%, Sigma–Aldrich) were used as received. Solvents were purchased from typical commercial sources at their highest purity and used without further treatment. Water was supplied from a Barnstead Nanopure Water System (18.3 MΩ cm).

Preparation of TiO_2 nanoparticles

TiO_2 nanoparticles were prepared by adopting a method reported previously [31]. In brief, titanium(IV)-*tert*-butoxide (0.182 g) was dissolved in 5 mL of water, and 0.791 g of 3-chloroaniline and 0.582 g of oleic acid were dissolved in 5 mL of toluene. Then the two solutions were added to a Teflon-lined autoclave and heated at 180 °C for 12 h. A white precipitate was produced at the bottom of the autoclave which was collected by centrifugation, washed with methanol several times, and dried under vacuum, affording purified TiO_2 nanoparticles.

Preparation of $AuTiO_2$ nanocomposites

$AuTiO_2$ nanocomposites were prepared by adopting a protocol described previously [32]. Experimentally, the TiO_2 nanoparticles prepared above (0.0755 g) were dispersed in 100 mL of tetrahydrofuran. Then a calculated amount of $HAuCl_4$ was added, followed by dropwise addition of a cold aqueous solution of sodium borohydride (10 molar excess as compared to gold), leading to an immediate color change from yellow to purple, signifying the formation of gold nanoparticles. The solution was subject to magnetic stirring at room temperature for about 1 h, followed by removal of tetrahydrofuran by rotary evaporation. The purple precipitates were dried under vacuum and denoted as $AuTiO_2$-pre.

The obtained $AuTiO_2$-pre then underwent hydrothermal treatment in the presence of ascorbic acid to produce oxygen vacancies. In a typical experiment, about 50 mg of $AuTiO_2$-pre was added into a Teflon-lined autoclave, along with a calculated amount of ascorbic acid and 10 mL of water. The mixture

was heated at 180 °C for 12 h. Four samples were prepared at the ascorbic acid:gold molar ratios of 0.5:1, 1:1, 2:1, and 3:1. The corresponding nanocomposites were denoted as $AuTiO_2$-I, $AuTiO_2$-II, $AuTiO_2$-III, and $AuTiO_2$-IV, respectively.

Characterizations

The sample morphologies were examined with a transmission electron microscope (TEM, Philips CM300) operated at 300 kV. X-ray photoelectron spectroscopic (XPS) measurements were carried out with a PHI 5400/XPS instrument equipped with an Al K_α source operated at 350 W and 10^{-9} Torr. Diffuse reflectance UV—vis spectra were acquired with a Perkin-Elmer Lambda 35 spectrometer. X-ray diffraction (XRD) measurements were performed with a Rigaku Miniflex powder diffractometer using Cu K_α radiation with a Ni filter ($\lambda = 0.154059$ nm at 30 kV and 15 mA) that features a detection limit of 0.04°.

Electron paramagnetic resonance (EPR)

For EPR measurements, samples were prepared by filling quartz EPR tubes (Wilmad, 4 mm outer diameter) with one centimeter of powdered materials, and centering the sample in the cavity resonator for data collection. Spectra were recorded at room temperature with a Bruker EMX EPR spectrometer operating at the X-band frequency (~9.4 GHz) using an ER 4122SHQE resonator (Bruker). All spectra were recorded at a power of 1 mW, a modulation amplitude of 1 G, and a modulation frequency of 100 KHz. Signal intensity was calculated as the peak-to-peak amplitude (S') of the EPR signal and double integration of the recorded signal. Progressive power saturation experiments were performed by recording spectra at various microwave powers between 0.063 and 63 mW. The data were analyzed by plotting S' vs. the square root of the microwave power.

Electrochemistry

Electrochemical experiments were carried out with a CHI 710 Electrochemical Workstation with a glassy-carbon disk and gold ring electrode, a platinum counter electrode, and a Ag/AgCl reference electrode. A catalyst ink was prepared by adding 10 mg of the $AuTiO_2$ nanocomposites prepared above and 40 mg of carbon black dispersed in 500 μL of ethanol and 5 μL of Nafion (corresponding to a nanocomposite concentration of 20 wt.%). The ink was then dropcast onto the glassy-carbon disk at a nanocomposite loading of ca. 20 μg, and dried in air before being immersed into electrolyte solutions for data acquisition. The Ag/AgCl electrode was calibrated against a reversible hydrogen electrode (RHE), and the potentials were all referred to this RHE electrode.

Results and discussion

Fig. 1 depicts two representative TEM micrographs of the $AuTiO_2$-III nanocomposites. From panel (A), it can be seen that gold nanoparticles, which appeared as dark-contrast objects, were embedded within a low-contrast matrix of TiO_2
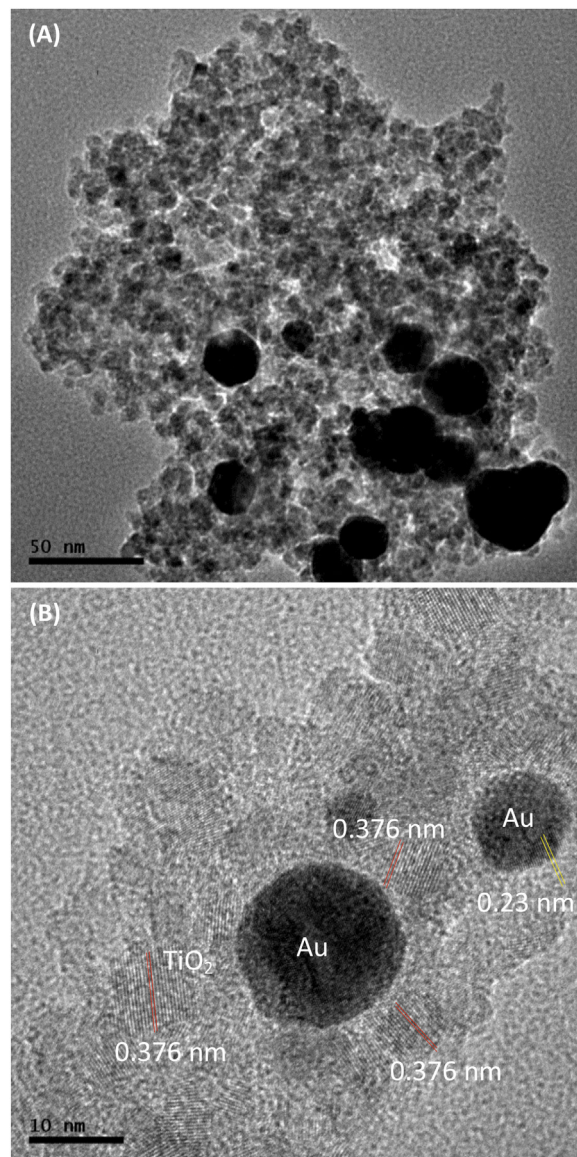

Fig. 1 — Representative TEM micrograph of $AuTiO_2$-III nanocomposites. Scale bars are (A) 50 nm and (B) 10 nm.

nanoparticles. The gold nanoparticles were somewhat polydisperse in size, ranging from 10 to 30 nm with an average diameter of 23.1 ± 5.2 nm, whereas the TiO_2 nanoparticles were much smaller, forming large-scale aggregates. From the high-resolution image in panel (B), one can see that the TiO_2 nanoparticles were markedly smaller at 5 to 10 nm in diameter, with well-defined lattice fringes where the interplanar spacing of 0.376 nm is consistent with that of anatase TiO_2 (101) planes (JCPDS no. 21-1272); and the gold nanoparticles were indeed in intimate contact with the TiO_2 nanoparticles, where the interplanar distance of 0.23 nm is in good agreement with the (111) crystalline planes of fcc Au (JCPDS no. 4-784). Consistent surface morphologies were observed with other $AuTiO_2$ nanocomposites in the series.

The structures of the $AuTiO_2$ nanocomposites were then characterized by XRD measurements. From Fig. 2, one can see
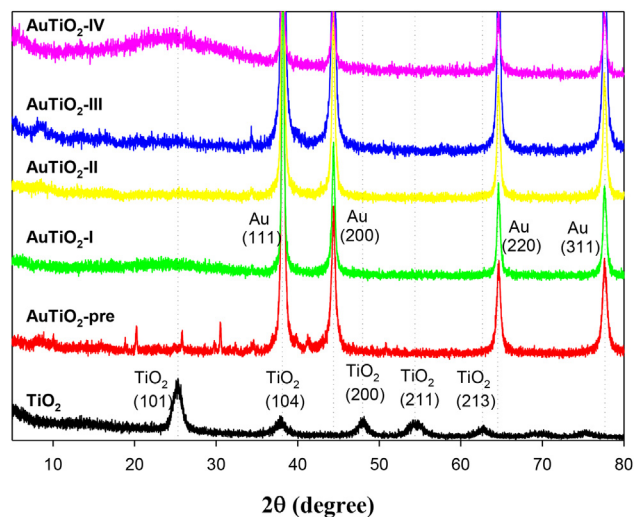
Fig. 2 – XRD spectra of TiO₂ and AuTiO₂ nanocomposites before and after hydrothermal treatment with ascorbic acid.

that prior to gold nanoparticle deposition, the TiO₂ nanoparticles exhibited a series of well-defined diffraction peaks at $2\theta = 25.3°, 38.1°, 48.0°, 54.5°$, and $63.0°$, corresponding to the (101), (104), (200), (211), and (213) crystalline planes of anatase TiO₂ (JCPDS no. 21-1272), respectively [33]. After gold nanoparticle deposition, the gold diffraction features (JCPDS no. 4-784) can be clearly identified for all AuTiO₂ nanocomposites at $2\theta = 38.3°$ for Au(111), $44.2°$ for Au(200), $64.5°$ for Au(220) and $77.6°$ for Au(311) [34]; and the TiO₂ (101) diffraction can also be resolved at $2\theta = 25.3°$, although it became increasingly broadened after hydrothermal treatment with the addition of an increasing amount of ascorbic acid, likely due to the formation of structural defects (oxygen vacancies), as manifested in XPS and EPR measurements (*vide infra*).

The formation of AuTiO₂ nanocomposites was further manifested in diffuse reflectance UV–vis measurements. From Fig. 3, one can see that TiO₂ colloids alone exhibit only a
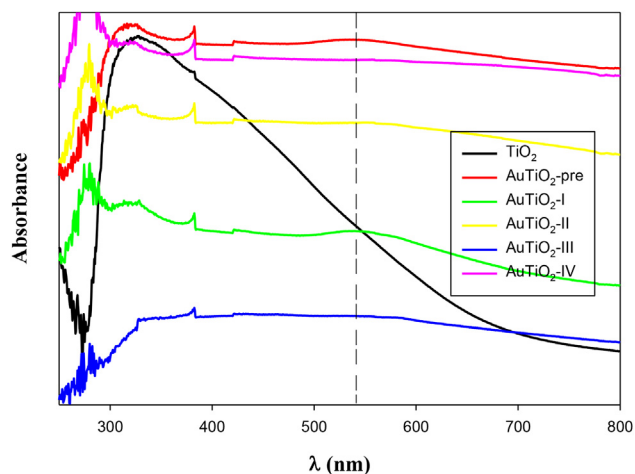

Fig. 3 – Diffuse reflectance UV–vis spectra of TiO₂ colloids and AuTiO₂ nanocomposites before and after hydrothermal treatment with ascorbic acid.

largely featureless absorption profile, and the extension of absorption down to 700 nm suggests the possible formation of bandgap states that arose from structural defects [35], considering the bandgap of anatase TiO₂ is about 3.2 eV [36]. After the deposition of gold nanoparticles onto TiO₂, the absorption was markedly enhanced in the visible range. In particular, the AuTiO₂ nanocomposites all exhibited a broad absorption peak centered at ca. 543 nm (marked by the dashed line). This can be ascribed to the surface plasmon resonance of gold nanoparticles [37] that were rather polydisperse in size and aggregated to some extent (Fig. 1). The results also suggest a similar structure of the gold nanoparticles within the series of nanocomposites before and after hydrothermal treatment with the addition of various amounts of ascorbic acid.

However, the nanocomposites exhibited a clear variation of the concentration of oxygen vacancies with the amount of ascorbic acid added in hydrothermal treatment, as revealed in EPR measurements. Fig. 4 depicts the EPR spectra of the series of AuTiO₂ nanocomposites. One can see that the prehydrothermal AuTiO₂–pre sample exhibited largely a featureless profile. In sharp contrast, after hydrothermal treatment with ascorbic acid, all nanocomposites showed a resonance transition centered at ca. 3370 G, with a corresponding g value of 2.003, which became increasingly intensified with an increasing amount of ascorbic aid added. This may be ascribed to the formation of unpaired electrons being trapped at the TiO₂ surface, consistent with results reported in earlier studies [26,30,35,38], due to partial reduction of Ti(IV) to Ti(III) by ascorbic acid [30,39,40]. Indeed, power saturation measurements of AuTiO₂-III (Fig. S1) show that the peak-to-peak derivative signal (S′) initially increased with the microwave power, reached a maximum at a power around 1 mW, and then decreased with a further increase of the microwave power, indicating that the signal reached saturation. The data was fitted to Eq. (1),

$$S' = K \frac{\sqrt{P}}{\left(1 + P/P_{1/2}\right)^{b/2}} \qquad (1)$$

where K is a constant, P is the incident microwave power, $P_{1/2}$ is the power at half saturation that is directly proportional to the spin-lattice (T_1) and spin-spin (T_2) relaxation rates [41], and b is a factor between 1 (for an inhomogeneous line) and 3 (for a purely homogenous line) [42]. A spin system that is easily saturated will have a low $P_{1/2}$ and a long relaxation rate. From the fitting, $P_{1/2}$ was estimated to be only 0.52 mW; such a low $P_{1/2}$ value is characteristic of trapped oxygen radicals [43–45]. Furthermore, one can see that the apparent oxygen vacancy concentration increased with the amounts of ascorbic acid added. This can be better manifested in the top inset to Fig. 4 which compared the amplitude difference in the EPR signals among the series of AuTiO₂ samples, as well as in the bottom inset which depicts the double integration of the respective spectrum. Both of these may be exploited for a rough estimation of how many species are causing the resonance signals [46]. From the results, one can see that the defect concentration (oxygen vacancies) increased in the order of AuTiO₂-pre ≤ AuTiO₂-II < AuTiO₂-I < AuTiO₂-III < AuTiO₂-IV.

Further structural insights into the elemental compositions and valence states of the series of the AuTiO₂
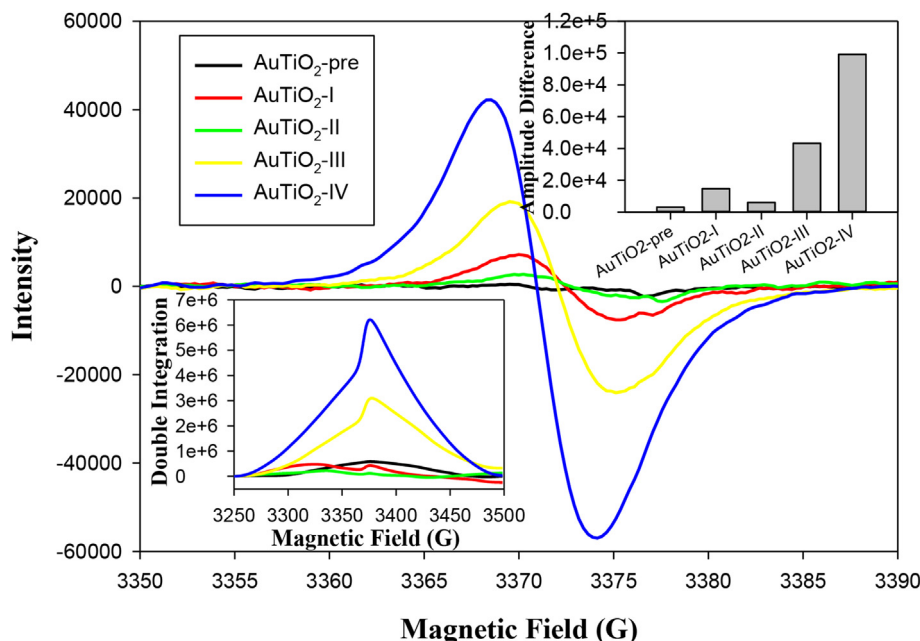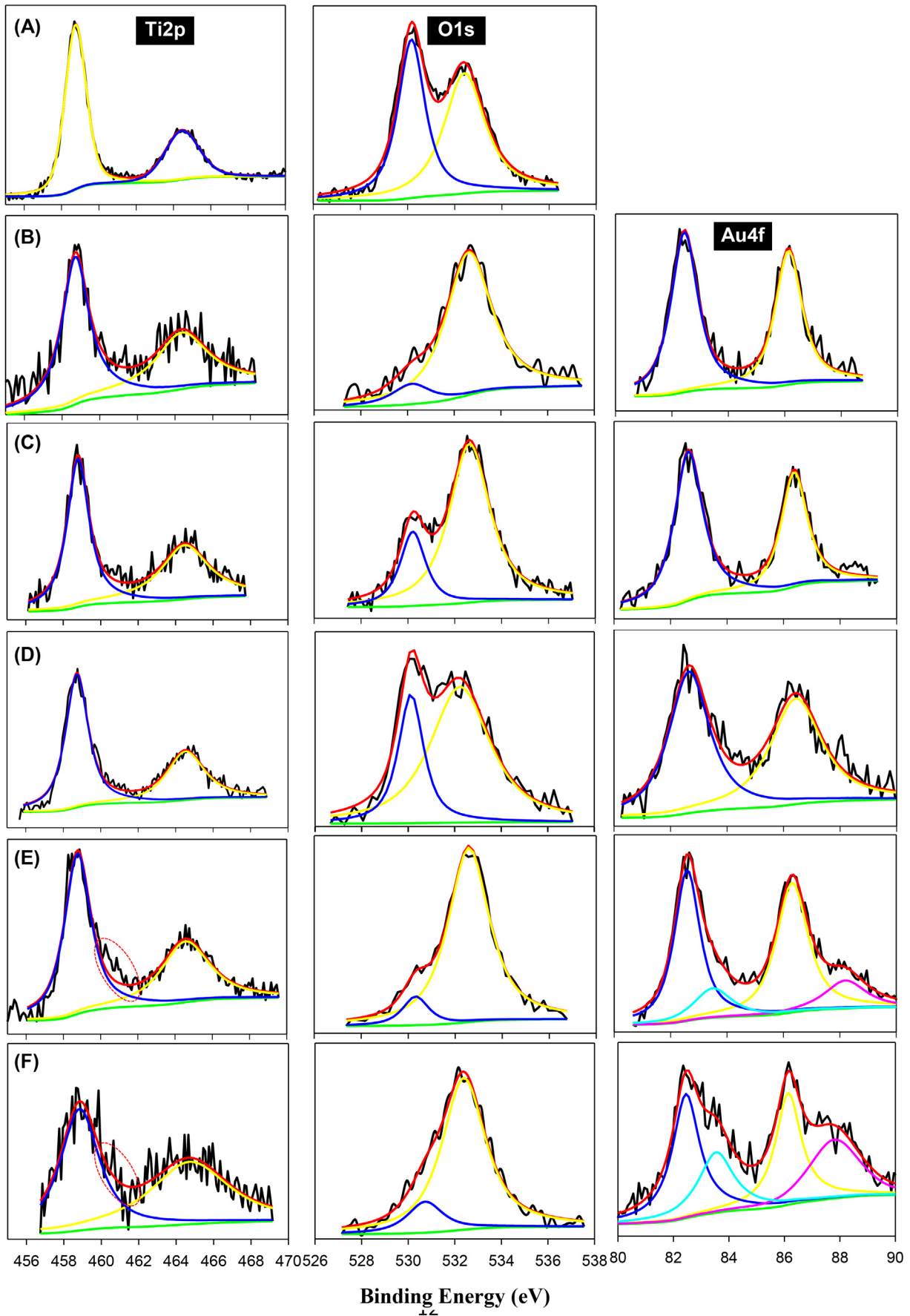
Fig. 4 − EPR spectra of the series of AuTiO$_2$ nanocomposites. Bottom inset is the double integration of the corresponding spectra, and top inset shows the variation of the amplitude difference with the ascorbic acid:gold feed ratio.

nanocomposites were unravelled by XPS measurements. From the survey spectra (Fig. S2), the Ti 2p, O 1s, and Au 4f electrons can be clearly identified with the AuTiO$_2$ nanocomposites at around 458, 530, and 85 eV (along with C 1s electrons at 285 eV), respectively. In high-resolution scans (Fig. 5), one can see that for all AuTiO$_2$ nanocomposites (panels (B) to (E)) the Ti 2p electrons appeared as a doublet at the binding energies of around 458.7 and 464.5 eV with a peak separation of 5.8 eV, consistent with those in TiO$_2$ colloids (panel (A)) [47]; and for the AuTiO$_2$-III and AuTiO$_2$-IV samples, there were some apparent deviations from deconvolution fits at around 460 eV (marked by the dashed circles), which might be ascribed to the Ti 2p$_{1/2}$ electrons of Ti(III) [48]. This is in good agreement with the EPR results where the concentrations of oxygen vacancies were markedly higher in these two samples than in the rest of the series (Fig. 4). For O 1s electrons, all samples (including TiO$_2$ colloids) exhibited two peaks at the binding energies of 530.4 and 532.6 eV. The former may be assigned to oxygen in TiO$_2$ whereas the latter is most likely due to hydroxyl groups adsorbed on the TiO$_2$ and/or Au surfaces [49]. For the Au 4f$_{7/2}$ electrons, the binding energy was rather consistent for all AuTiO$_2$ nanocomposites at ca. 82.5 eV (with Au 4f$_{5/2}$ at 86.3 eV), which was markedly lower than that (84.0 eV) typically observed with bulk gold and gold nanoparticles [50]. This signifies electron-rich gold, likely due to excess NaBH$_4$ used in nanoparticle synthesis as well as hydrothermal treatment in the presence of reductive ascorbic acid. Such a low binding energy for Au 4f electrons has been reported previously, for instance, with Au nanoparticles supported on TiO$_2$-MO$_x$ (M = Fe, Co, Zn) and ascribed to effective charge transfer from the oxides to gold [51], as well as with TiO$_2$-supported AuPd alloy nanoparticles that were subjected to a thermal treatment in a H$_2$ atmosphere [52]. For AuTiO$_2$-III and AuTiO$_2$-IV, the appreciable concentrations of oxygen

vacancies (Fig. 4) further enhanced the electron density on Au that likely facilitated the adsorption of hydroxyl groups, as evidenced by a second pair of Au 4f peaks at somewhat higher energies of 83.3 and 88.5 eV [53]. Furthermore, based on the integrated peak areas, the Au:Ti atomic ratio was found to be rather consistent at 11% for all the AuTiO$_2$ nanocomposites.

The electrocatalytic activity of the nanocomposites prepared above were then examined by electrochemical measurements in alkaline media. Fig. S3 depicts the steady-state cyclic voltammograms of the nanocomposites loaded onto a glassy carbon electrode in a N$_2$-saturated 0.1 M NaOH solution at the potential scan rate of 100 mV s^{-1}. It can be seen that in contrast to TiO$_2$ colloids that exhibited only a featureless voltammetric profile due to double-layer capacitance charging [19,32], the series of AuTiO$_2$ nanocomposites all showed a pair of voltammetric peaks, where the anodic peak at around +1.3 V can be ascribed to electrochemical oxidation of gold and the cathodic peak at ca. +1.0 V to the reduction of gold oxides. Furthermore, based on the integrated peak areas of gold oxide reduction, the effective electrochemical surface area was estimated to be rather consistent at 0.22 cm^2 for AuTiO$_2$-pre, 0.13 cm^2 for AuTiO$_2$-I, 0.12 cm^2 for AuTiO$_2$-II, 0.71 cm^2 for AuTiO$_2$-III, and 0.30 cm^2 for AuTiO$_2$-IV [54].

The AuTiO$_2$ nanocomposites were then evaluated for their electrocatalytic activity towards ORR. Fig. 6(A) shows the RRDE measurements in an O$_2$ saturated 0.1 M NaOH solution at the rotation rate of 1600 rpm. One can see that for all samples, nonzero cathodic currents at the disk electrode emerged at sufficiently negative electrode potentials, suggesting apparent electrocatalytic activity towards ORR, despite the relatively large size of the Au nanoparticles (Fig. 1). However, the performance was markedly different among the series of samples. For instance, the onset potential for TiO$_2$ nanoparticles was estimated to be +0.73 V; yet for the AuTiO$_2$
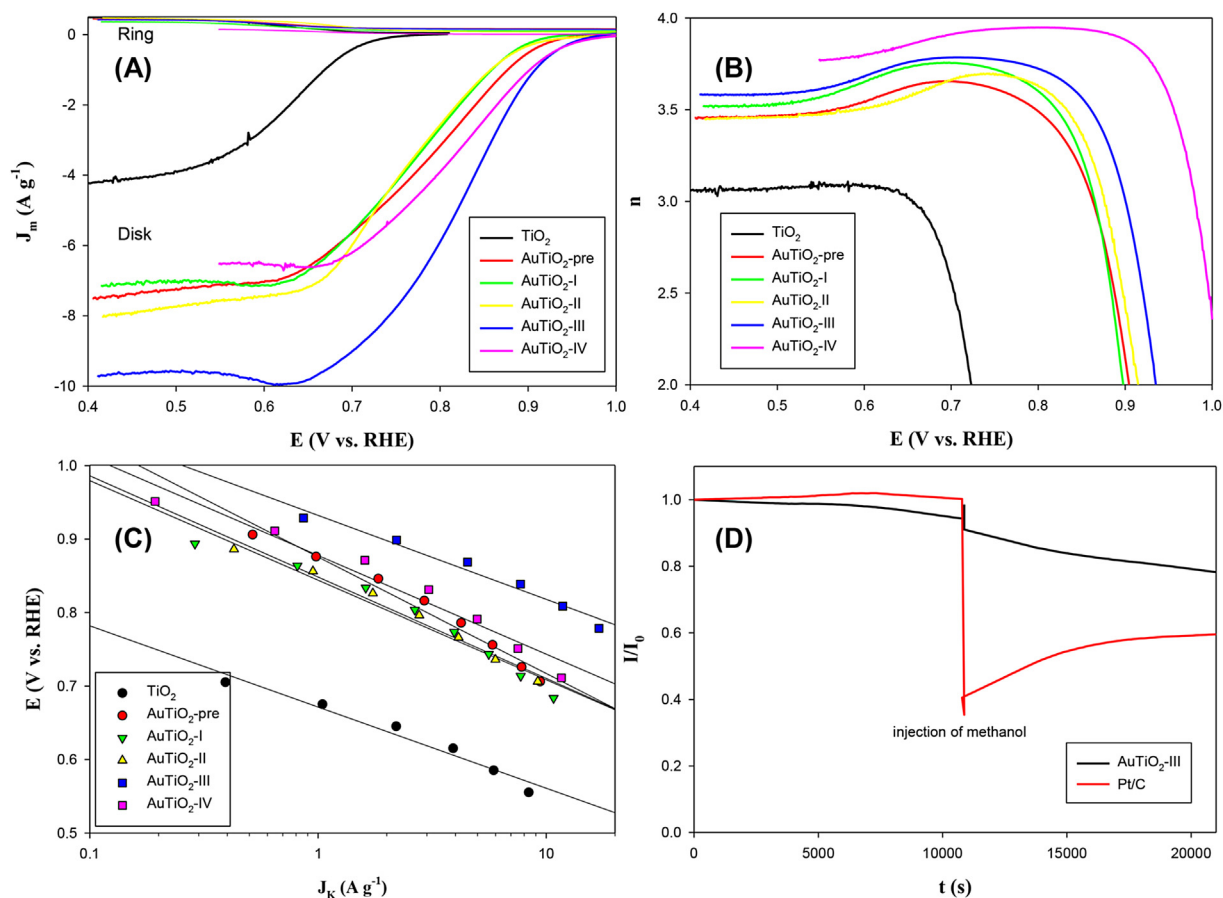
Fig. 6 – (A) RRDE voltammograms of a glassy carbon electron modified with TiO_2 and $AuTiO_2$ nanocomposites in an oxygen-saturated 0.1 M NaOH solution. Potential scan rate 10 mV s^{-1} and rotation rate 1600 rpm. Catalyst loadings 20 μg of composite. **(B)** Variation of the number of electron transfer (n) with electrode potential. Data were obtained from the voltammograms in panel (A). **(C)** Tafel plots of the various nanocomposite catalysts. **(D)** Chronoamperometric profiles of $AuTiO_2$-III and Pt/C catalysts in an oxygen-saturated 0.1 M NaOH solution at the electrode potential of +0.60 V, where 1 M methanol was injected into the electrolyte solution at t = 3 h.

nanocomposites, the onset potentials were far more positive by ca. 200 mV, at +0.92 V for $AuTiO_2$-pre, $AuTiO_2$-I and $AuTiO_2$-II, and +0.95 V for $AuTiO_2$-III and $AuTiO_2$-IV, indicating marked enhancement of the catalytic performance by the incorporation of gold nanoparticles onto TiO_2. Significant discrepancy can also be seen in the diffusion limiting currents. For instance, at +0.60 V and 1600 rpm, the current density (J_m, voltammetric currents normalized to the composite loading) can be found at 2.67 A g^{-1} for TiO_2, but increased by more than two folds to 7.04 A g^{-1} for $AuTiO_2$-pre, 7.13 A g^{-1} for $AuTiO_2$-I, 7.46 A g^{-1} for $AuTiO_2$-II, 9.89 A g^{-1} for $AuTiO_2$-III, and 6.55 A g^{-1} for $AuTiO_2$-IV. Taken together, these results suggest that the $AuTiO_2$-III nanocomposites stood out as the best catalysts among the series.

Furthermore, by setting the ring electrode at +1.5 V, collection experiments showed that the ring currents were at least one order of magnitude lower than those at the disk,

indicating only a minimal amount of peroxide species were produced during oxygen reduction. In fact, the number of electron transfer (n) may be quantified by Eq. (2),

$$n = \frac{4I_D}{I_D + I_R/N} \tag{2}$$

where I_D and I_R are the voltammetric currents at the disk and ring electrodes, respectively, and N is the collection efficiency (0.40) [55]. From panel (B), one can see that within the potential range of +0.4 to +1.0 V, the n values increase in the order of TiO_2 < $AuTiO_2$-pre ≈ $AuTiO_2$-II < $AuTiO_2$-I < $AuTiO_2$-III < $AuTiO_2$-IV. For instance, at +0.60 V, n = 3.13 for TiO_2, 3.58 for $AuTiO_2$-pre, 3.68 for $AuTiO_2$-I, 3.54 for $AuTiO_2$-II, 3.71 for $AuTiO_2$-III, and 3.81 for $AuTiO_2$-IV, corresponding to a H_2O_2 yield of 34.8%, 16.8%, 12.8%, 18.4%, 11.6%, and 7.6%. That is, with the formation of $AuTiO_2$ nanocomposites, the H_2O_2 yield decreased significantly and the ORR proceeded mostly by the

Fig. 5 – XPS spectra of Ti2p O1s and Au4f electrons of (A) TiO_2, (B) $AuTiO_2$-pre, (C) $AuTiO_2$-I, (D) $AuTiO_2$-II, (E) $AuTiO_2$-III, and (F) $AuTiO_2$-IV. Black curves are experimental data and colored curves are deconvolution fits. (For interpretation of the references to colour in this figure legend, the reader is referred to the web version of this article.)

four-electron reduction pathway, $O_2 + 2H_2O + 4e \rightarrow 4OH^-$ [11,56].

Further insights into the ORR electron transfer kinetics can be obtained from analysis and comparison of the Tafel plots, where the kinetic current density (J_k) was quantified by the y-axis intercepts of the respective Koutecky-Levich plots [57]. From panel (C), it can be seen that for all nanocomposite catalysts, the kinetic current densities increased with increasingly negative electrode potential, and within the potential range of +0.95 to +0.55 V, AuTiO$_2$-III exhibited the highest kinetic current density, whereas TiO$_2$ the lowest, with the rest of the samples showing similar activity in the intermediate range. For instance, at +0.90 V, the kinetic current density was only 0.40 A g^{-1} for AuTiO$_2$-I, 0.43 A g^{-1} for AuTiO$_2$-II, 0.70 A g^{-1} for AuTiO$_2$-pre, 0.71 A g^{-1} for AuTiO$_2$-IV, and 1.96 A g^{-1} for AuTiO$_2$-III (only minimal activity for TiO$_2$ at this potential).

In addition, one may note that the Tafel slope of the series of sample was actually very close at 110 mV dec^{-1} for TiO$_2$, 158 mV dec^{-1} for AuTiO$_2$-pre, 136 mV dec^{-1} for AuTiO$_2$-I, 136 mV dec^{-1} for AuTiO$_2$-II, 114 mV dec^{-1} for AuTiO$_2$-III, and 134 mV dec^{-1} for AuTiO$_2$-IV. This implies a similar ORR mechanism for this series of AuTiO$_2$ catalysts where the rate-determining step was likely the first electron reduction of oxygen [11,12].

For metal—metal oxide nanocomposites [11,12], it has been known that the electronic interactions at the interface likely play a key role in determining the bonding interactions with oxygen species and hence the ORR activity. In the present study, the discrepancy of the ORR performances observed above may be accounted for by the impacts of oxygen vacancies on the adsorption of oxygen intermediates on the composite surfaces. The AuTiO$_2$-III and AuTiO$_2$-IV samples, which exhibited markedly higher ORR activity than other samples in the series, also showed significantly higher concentrations of oxygen vacancies (Fig. 4). This most likely led to enhanced adsorption of oxygen species onto the nanocomposites, due to partial charge transfer to Au from oxygen-deficient TiO$_2$ (Fig. 5) [58]. Importantly, the results presented above suggest an optimal concentration of oxygen vacancies for maximal ORR activity, as manifested by the AuTiO$_2$-III sample which stood out as the best catalyst among the series. This may be accounted for by the fact that whereas oxygen vacancies enhanced bonding interactions between oxygen and the nanocomposites, too strong binding would actually diminish the ORR performance, as manifested by the so-called volcano plot [59].

It should be noted that the ORR performance of the AuTiO$_2$ nanocomposites observed above was markedly enhanced in comparison with similar composite catalysts that were not treated hydrothermally with ascorbic acid (Table S1), within the context of onset potential, n value, and kinetic current density. This suggests that controlled formation of oxygen vacancies may be exploited as a unique, powerful parameter in the deliberate manipulation of the nanocomposite ORR activity [11,12]. Notably, the electrocatalytic activity of AuTiO$_2$-III was rather comparable to that of commercial Pt/C catalysts [1,2]. In addition, the AuTiO$_2$ nanocomposites and Pt/C both exhibited excellent stability, where the ORR currents remained virtually invariant after continuous operation at

+0.60 V for ca. 3 h, as depicted in panel (D). One can also see that AuTiO$_2$ showed much better tolerance against methanol poisoning than Pt/C. For instance, upon the injection of 1 M methanol into the electrolyte solution, the ORR current at the Pt/C catalysts dropped by ca. 60% whereas only a 4% decrease was observed with AuTiO$_2$-III.

Conclusions

In this study, gold-TiO$_2$ nanocomposites were prepared by chemical deposition of gold nanoparticles onto TiO$_2$ colloid surface. Hydrothermal treatment at a controlled temperature in the presence of ascorbic acid led to the generation of oxygen vacancies where the concentration varied with the amount of ascorbic acid added. This led to a deliberate manipulation of the electrocatalytic activity towards oxygen reduction in alkaline media. Voltammetric measurements showed that the nanocomposites with a relatively high concentration of oxygen vacancies exhibited the best ORR activity among the series, as a result of deliberate manipulation of the binding interactions of oxygen species on the nanocomposite surfaces that was facilitated by partial charge transfer from oxygen-deficient TiO$_2$ to gold. The results further highlight the significance of metal-substrate interfacial interactions in the design and engineering of functional nanocomposites as effective catalysts for fuel cell electrochemistry.

Acknowledgments

Appendix A. Supplementary data

Supplementary data related to this article can be found at http://dx.doi.org/10.1016/j.ijhydene.2016.07.232.

REFERENCES

[1] Wang YG, Yoon Y, Glezakou VA, Li J, Rousseau R. The role of reducible oxide-metal cluster charge transfer in catalytic processes: new insights on the catalytic mechanism of CO oxidation on Au/TiO$_2$ from ab initio molecular dynamics. J Am Chem Soc 2013;135:10673—83.

[2] Liu X, Liu MH, Luo YC, Mou CY, Lin SD, Cheng H, et al. Strong metal-support interactions between gold nanoparticles and ZnO nanorods in CO oxidation. J Am Chem Soc 2012;134:10251—8.

[3] Jaksic MM, Botton GA, Papakonstantinou GD, Nan FH, Jaksic JM. Primary oxide latent storage and spillover enabling electrocatalysts with reversible oxygen electrode properties and the alterpolar revertible (PEMFC versus WE) cell. J Phys Chem C 2014;118:8723–46.

[4] Sener T, Demirci UB, Gul OF, Ata A. Pd-MnO_2-Fe_2O_3/C as electrocatalyst for the formic acid electrooxidation. Int J Hydrogen Energy 2015;40:6920–6.

[5] Duan ZY, Henkelman G. CO oxidation at the Au/TiO_2 boundary: the role of the Au/Ti-5c site. ACS Catal 2015;5:1589–95.

[6] Widmann D, Behm RJ. Activation of molecular oxygen and the nature of the active oxygen species for CO oxidation on oxide supported Au catalysts. Acc Chem Res 2014;47:740–9.

[7] Fu Q, Li WX, Yao YX, Liu HY, Su HY, Ma D, et al. Interface-confined ferrous centers for catalytic oxidation. Science 2010;328:1141–4.

[8] Neophytides SG, Zafeiratos S, Papakonstantinou GD, Jaksic JM, Paloukis FE, Jaksic MM. Extended Brewer hypo-hyper-d-interionic bonding theory II. Strong metal-support interaction grafting of composite electrocatalysts. Int J Hydrogen Energy 2005;30:393–410.

[9] Cheng NC, Liu J, Banis MN, Geng DS, Li RY, Ye SY, et al. High stability and activity of Pt electrocatalyst on atomic layer deposited metal oxide/nitrogen-doped graphene hybrid support. Int J Hydrogen Energy 2014;39:15967–74.

[10] Comotti M, Li WC, Spliethoff B, Schuth F. Support effect in high activity gold catalysts for CO oxidation. J Am Chem Soc 2006;128:917–24.

[11] Lin C, Song Y, Cao L, Chen S. Oxygen reduction catalyzed by Au-TiO_2 nanocomposites in alkaline media. ACS Appl Mater Interfaces 2013;5:13305–11.

[12] Chen W, Ny D, Chen S. SnO_2–Au hybrid nanoparticles as effective catalysts for oxygen electroreduction in alkaline media. J Power Sources 2010;195:412–8.

[13] Ma Z, Dai S. Chapter 1. Stabilizing gold nanoparticles by solid supports. In: Ma Z, Dai S, editors. Heteroenous gold catalysts and catalysis. Royal of Society of Chemistry; 2014. p. 1–26.

[14] Wu B, Zheng N. Surface and interface control of noble metal nanocrystals for catalytic and electrocatalytic applications. Nano Today 2013;8:168–97.

[15] Melvin AA, Bharad PA, Illath K, Lawrence MP, Gopinath CS. Is there any real effect of low dimensional morphologies towards light harvesting? A case study of Au–rGO-TiO_2 nanocomposites. ChemistrySelect 2016;5:917–23.

[16] Horvath A, Beck A, Sarkany A, Stefler G, Varga Z, Geszti O, et al. Silica-supported Au nanoparticles decorated by TiO_2: formation, morphology, and CO oxidation activity. J Phys Chem B 2006;110:15417–25.

[17] Ma Z, Brown S, Howe JY, Overbury SH, Dai S. Surface modification of Au/TiO_2 catalysts by SiO_2 via atomic layer deposition. J Phys Chem C 2008;112:9448–57.

[18] Huang X, Guo C, Zuo J, Zheng N, Stucky GD. An assembly route to inorganic catalytic nanoreactors containing sub-10-nm gold nanoparticles with anti-aggregation properties. Small 2009;5:361–5.

[19] Kim J-H, Ishihara A, Mitsushima S, Kamiya N, Ota K-I. Catalytic activity of titanium oxide for oxygen reduction reaction as a non-platinum catalyst for PEFC. Electrochim Acta 2007;52:2492–7.

[20] Cerri I, Nagami T, Davies J, Mormiche C, Vecoven A, Hayden B. Innovative catalyst supports to address fuel cell stack durability. Int J Hydrogen Energy 2013;38:640–5.

[21] Kim J-H, Chang S, Kim Y-T. Compressive strain as the main origin of enhanced oxygen reduction reaction activity for Pt electrocatalysts on chromium-doped titania support. Appl Catal B Environ 2014;158–159:112–8.

[22] Wang N, Niu WH, Li LG, Liu J, Tang ZH, Zhou WJ, et al. Oxygen electroreduction promoted by quasi oxygen vacancies in metal oxide nanoparticles prepared by photoinduced chlorine doping. Chem Commun 2015;51:10620–3.

[23] Myung JH, Shin TH, Huang XB, Carins G, Irvine JTS. Enhancement of redox stability and electrical conductivity by doping various metals on ceria, $Ce_{1-x}M_xO_{2-delta}$ (M = Ni, Cu, Co, Mn, Ti, Zr). Int J Hydrogen Energy 2015;40:12003–8.

[24] Zana A, Rüdiger C, Kunze-Liebhäuser J, Granozzi G, Reeler NEA, Vosch T, et al. Core-shell TiO_2@C: towards alternative supports as replacement for high surface area carbon for PEMFC catalysts. Electrochim Acta 2014;139:21–8.

[25] Esfandiar A, Irajizad A, Akhavan O, Ghasemi S, Gholami MR. Pd-WO_3/reduced graphene oxide hierarchical nanostructures as efficient hydrogen gas sensors. Int J Hydrogen Energy 2014;39:8169–79.

[26] Pan X, Yang MQ, Fu X, Zhang N, Xu YJ. Defective TiO_2 with oxygen vacancies: synthesis, properties and photocatalytic applications. Nanoscale 2013;5:3601–14.

[27] Linh NH, Nguyen TQ, Diño WA, Kasai H. Effect of oxygen vacancy on the adsorption of O_2 on anatase TiO_2(001): a DFT-based study. Surf Sci 2015;633:38–45.

[28] Aschauer U, Chen J, Selloni A. Peroxide and superoxide states of adsorbed O_2 on anatase TiO_2(101) with subsurface defects. Phys Chem Chem Phys 2010;12:12956–60.

[29] Zhu Q, Peng Y, Lin L, Fan C-M, Gao G-Q, Wang R-X, et al. Stable blue TiO_{2-x} nanoparticles for efficient visible light photocatalysts. J Mater Chem A 2014;2:4429.

[30] Wajid Shah M, Zhu Y, Fan X, Zhao J, Li Y, Asim S, et al. Facile synthesis of defective TiO_{2-x} nanocrystals with high surface area and tailoring bandgap for visible-light photocatalysis. Sci Rep 2015;5:15804.

[31] Pan DC, Zhao NN, Wang Q, Jiang SC, Ji XL, An LJ. Facile synthesis and characterization of luminescent TiO_2 nanocrystals. Adv Mater 2005;17:1991–5.

[32] Liu K, Song Y, Chen SW. Defective TiO_2-supported Cu nanoparticles as efficient and stable electrocatalysts for oxygen reduction in alkaline media. Nanoscale 2015;7:1224–32.

[33] Antić Ž, Krsmanović RM, Nikolić MG, Marinović-Cincović M, Mitrić M, Polizzi S, et al. Multisite luminescence of rare earth doped TiO_2 anatase nanoparticles. Mater Chem Phys 2012;135:1064–9.

[34] Nakamoto M, Yamamoto M, Fukusumi M. Thermolysis of gold(i) thiolate complexes producing novel gold nanoparticles passivated by alkyl groups. Chem Commun 2002;1622–3.

[35] Pan XY, Xu Y-J. Fast and spontaneous reduction of gold ions over oxygen-vacancy-rich TiO_2: a novel strategy to design defect-based composite photocatalyst. Appl Catal A Gen 2013;459:34–40.

[36] Dette C, Perez-Osorio MA, Kley CS, Punke P, Patrick CE, Jacobson P, et al. TiO_2 anatase with a bandgap in the visible region. Nano Lett 2014;14:6533–8.

[37] Abd-Ellah M, Moghimi N, Zhang L, Thomas JP, McGillivray D, Srivastava S, et al. Plasmonic gold nanoparticles for ZnO-nanotube photoanodes in dye-sensitized solar cell application. Nanoscale 2016;8:1658–64.

[38] Pan X, Xu Y-J. Defect-mediated growth of noble-metal (Ag, Pt, and Pd) nanoparticles on TiO_2 with oxygen vacancies for photocatalytic redox reactions under visible light. J Phys Chem C 2013;117:17996–8005.

[39] Naldoni A, D'Arienzo M, Altomare M, Marelli M, Scotti R, Morazzoni F, et al. Pt and Au/TiO_2 photocatalysts for methanol reforming: role of metal nanoparticles in tuning charge trapping properties and photoefficiency. Appl Catal B Environ 2013;130–131:239–48.

[40] Randorn C, Irvine JTS. Synthesis and visible light photoactivity of a high temperature stable yellow TiO_2 photocatalyst. J Mater Chem 2010;20:8700.

[41] Altenbach C, Flitsch SL, Khorana HG, Hubbell WL. Structural studies on transmembrane proteins .2. Spin labeling of bacteriorhodopsin mutants at unique cysteines. Biochemistry 1989;28:7806–12.

[42] Galli C, MacArthur R, AbuSoud HM, Clark P, Stuehr DJ, Brudvig GW. EPR spectroscopic characterization of neuronal NO synthase. Biochemistry 1996;35:2804–10.

[43] Ahmad R, Kuppusamy P. Theory, instrumentation, and applications of electron paramagnetic resonance oximetry. Chem Rev 2010;110:3212–36.

[44] Baumann SO, Elser MJ, Auer M, Bernardi J, Husing N, Diwald O. Solid solid interface formation in TiO_2 nanoparticle networks. Langmuir 2011;27:1946–53.

[45] Pascutti PG, Ito AS. EPR study of melanin protein-interaction - photoinduced free-radicals and progressive microwave-power saturation. J Photochem Photobiol B Biol 1992;16:257–66.

[46] Judeikis HS. Errors in the evaluation of moments of a paramagnetic resonance line. J Appl Phys 1964;35:2615.

[47] Palanisamy B, Babu CM, Sundaravel B, Anandan S, Murugesan V. Sol-gel synthesis of mesoporous mixed Fe_2O_3/TiO_2 photocatalyst: application for degradation of 4-chlorophenol. J Hazard Mater 2013;252–253:233–42.

[48] Wang Y, Sun H, Tan S, Feng H, Cheng Z, Zhao J, et al. Role of point defects on the reactivity of reconstructed anatase titanium dioxide (001) surface. Nat Commun 2013;4:2214.

[49] Zoulalian V, Zurcher S, Tosatti S, Textor M, Monge S, Robin JJ. Self-assembly of poly(ethylene glycol)-poly(alkyl phosphonate) terpolymers on titanium oxide surfaces: synthesis, interface characterization, investigation of nonfouling properties, and long-term stability. Langmuir 2010;26:74–82.

[50] Melvin AA, Illath K, Das T, Raja T, Bhattacharyya S, Gopinath CS. M-Au/TiO_2 (M = Ag, Pd, and Pt) nanophotocatalyst for overall solar water splitting: role of interfaces. Nanoscale 2015;7:13477–88.

[51] Chang FW, Yu HY, Roselin LS, Yang HC, Ou TC. Hydrogen production by partial oxidation of methanol over gold catalysts supported on TiO_2-MO_x (M = Fe, Co, Zn) composite oxides. Appl Catal A Gen 2006;302:157–67.

[52] Morad M, Sankar M, Cao EH, Nowicka E, Davies TE, Miedziak PJ, et al. Solvent-free aerobic oxidation of alcohols using supported gold palladium nanoalloys prepared by a modified impregnation method. Catal Sci Technol 2014;4:3120–8.

[53] Yang K, Zhang YF, Li Y, Huang P, Chen X, Dai WX, et al. Insight into the function of alkaline earth metal oxides as electron promoters for Au/TiO_2 catalysts used in CO oxidation. Appl Catal B Environ 2016;183:206–15.

[54] Trasatti S, Petrii OA. Real surface-area measurements in electrochemistry. Pure Appl Chem 1991;63:711–34.

[55] Zhou ZY, Kang XW, Song Y, Chen SW. Enhancement of the electrocatalytic activity of Pt nanoparticles in oxygen reduction by chlorophenyl functionalization. Chem Commun 2012;48:3391–3.

[56] Jašin D, Abu-Rabi A, Mentus S, Jovanović D. Oxygen reduction reaction on spontaneously and potentiodynamically formed Au/TiO_2 composite surfaces. Electrochim Acta 2007;52:4581–8.

[57] Hu PG, Song Y, Chen LM, Chen SW. Electrocatalytic activity of alkyne-functionalized AgAu alloy nanoparticles for oxygen reduction in alkaline media. Nanoscale 2015;7:9627–36.

[58] Tan S-j, Wang B. Active sites for adsorption and reaction of molecules on rutile TiO_2(110) and anatase TiO_2(001) surfaces. Chin J Chem Phys 2015;28:383–95.

[59] Sabatier P. Announcement. Hydrogenation and dehydrogenation for catalysis. Ber Dtsch Chem Ges 1911;44:1984–2001.